Journal of Clinical and Translational Hepatology **2022**
DOI: 10.14218/JCTH.2021.00580

Original Article

MRI/PAI Dual-modal Imaging-guided Precise Tracking of Bone Marrow-derived Mesenchymal Stem Cells Labeled with Nanoparticles for Treating Liver Cirrhosis

Feng-Yong Liu[1,2,3], Ming Shi[2], Xin Li[3], Hong-Jun Yuan[3], Xiao-Mei Tian[1,3], Yi-Mao Xia[1,3], Min Zhou[4] and Fu-Sheng Wang[1,2*]

[1]Chinese PLA Medical School, Beijing, China; [2]Senior Department of Infectious Diseases, Fifth Medical Center of PLA General Hospital, Beijing, China; [3]Department of Interventional Radiology, Senior Department of Oncology, Fifth Medical Center of PLA General Hospital, Beijing, China; [4]Institute of Translational Medicine, Zhejiang University, Hangzhou, Zhejiang, China.

Received: 23 December 2021 | **Revised:** 24 March 2022 | **Accepted:** 5 May 2022 | **Published:** 27 May 2022

Abstract

Background and Aims: Stem cell transplantation is a potential treatment option for liver cirrhosis (LC). Accurately and noninvasively monitoring the distribution, migration, and prognosis of transplanted stem cells using imaging methods is important for in-depth study of the treatment mechanisms. Our study aimed to develop Au-Fe_3O_4 silica nanoparticles (NPs) as tracking nanoplatforms for dual-modal stem cell imaging. ***Methods:*** Au-Fe_3O_4 silica NPs were synthesized by seed-mediated growth method and co-precipitation. The efficiency and cytotoxicity of the NPs-labeled bone marrow-derived mesenchymal stem cells (BM-MSCs) were evaluated by Cell Counting Kit-8 assays, ICP-MS, phenotypic characterization, and histological staining. The biodistribution of labeled BM-MSCs injected through different routes (the hepatic artery or tail vein) into rats with LC was detected by magnetic resonance imaging (MRI), photoacoustic imaging (PAI), and Prussian blue staining. ***Results:*** Synthesized Au-Fe_3O_4 silica NPs consisted of a core (star-shaped Au NPs) and an outside silica layer doped with Fe_3O_4 NPs. After 24 h coincubation with 2.0 OD concentration of NPs, the viability of BM-MSCs was 77.91%±5.86% and the uptake of Au and Fe were (22.65±1.82) μg/mL and (234.03±11.47) μg/mL, respectively. The surface markers of labeled BM-MSCs unchanged significantly. Labeled BM-MSCs have osteogenic and adipogenic differentiation potential. Post injection *in vivo*, rat livers were hypointense on MRI and hyperintense on PAI. Prussian blue staining showed that more labeled BM-MSCs accumulated in the liver of the hepatic artery group. The severity of LC of the rats in the hepatic artery group was significantly alleviated. ***Conclusions:*** Au-Fe_3O_4 silica NPs were suitable MRI/PAI dual-modal imaging nanoplatforms for stem cell tracking in regenerative medicine. Transhepatic arterial infusion of BM-MSCs was the optimal route for the treatment of LC.

Citation of this article: Liu FY, Shi M, Li X, Yuan HJ, Tian XM, Xia YM, *et al*. MRI/PAI Dual-modal Imaging-guided Precise Tracking of Bone Marrow-derived Mesenchymal Stem Cells Labeled with Nanoparticles for Treating Liver Cirrhosis. J Clin Transl Hepatol 2022. doi: 10.14218/JCTH.2021.00580.

Introduction

Liver cirrhosis (LC) is a chronic disease that affects 1% of the world population.[1] Due to the compensatory ability of the liver, most patients are diagnosed at the middle and advanced stages, which are generally accompanied by fatal complications, including portal hypertension, hepatic encephalopathy, renal failure, severe ascites, giant spleen, and repeated bacterial infections.[2,3] Although liver transplantation treats cirrhosis, limitations such as a shortage of liver donors, immune rejection, recurrence, and high costs significantly impede its clinical application.[4,5]

Mesenchymal stem cells (MSCs), derived from adult stem cells, are found in adipose, umbilical cord blood, peripheral blood, brain, skeletal muscle, and other tissues.[6,7] They are easily isolated, cultured, and stored, enhancing their clinical applications.[8–10] Additionally, the low expression (positive rate ≤2%) of cell surface markers such as CD45, CD34, and CD14/CD11b may significantly reduce the host immune response against MSCs.[11] Existing data demonstrates the great potential of MSCs as cell replacement therapy for LC.[12,13] However, because survival, migration, homing, and functions of these cells after transplanting into the liver are unclear, their use as therapeutic agents for LC remains unexplored. To address these issues, reliable, noninvasive, real-time stem cell tracking and imaging techniques are urgently needed.

Various nanomaterials are used for stem cell imaging and tracking. For instance, image platforms based on Au and Iron oxide (Fe_3O_4) nanoparticles (NPs) are the most common. Au NPs have many advantages, including high plasticity and safety.[14] Moreover, they absorb near-infrared light and generate photoacoustic signals, allowing precise

Keywords: Bone marrow-derived mesenchymal stem cells; Liver cirrhosis; Dual-modal imaging; Stem cell tracking; Nanoparticles.

Abbreviations: BM-MSCs, bone marrow-derived mesenchymal stem cells; LC, liver cirrhosis; MRI, magnetic resonance imaging; MSCs, mesenchymal stem cells; NPs, nanoparticles; PAI, photoacoustic imaging.

***Correspondence to:** Fu-Sheng Wang, Senior Department of Infectious Diseases, Fifth Medical Center of PLA General Hospital, Beijing 100039, China. ORCID: https://orcid.org/0000-0002-8043-6685. Tel: +86-15801502008, Fax: +86-10-66933332, E-mail: fswang302@163.com

photoacoustic imaging (PAI).[15,16] Fe_3O_4 NPs are widely employed as magnetic resonance imaging (MRI) T_2 contrast agents because of their excellent relaxation efficiency and biocompatibility.[17,18] This study aimed to develop composite Au and Fe_3O_4 NPs. The NPs labeled BM-MSCs, which allowed MRI/PAI dual-model imaging. The properties should allow accurate tracking of BM-MSCs when treating LC.

Methods

Preparation of Au-Fe_3O_4 silica NPs

Sodium citrate, chloroauric acid, and ferrous chloride were obtained from Shanghai Aladdin Biochemical Technology Co., Ltd (China). Au NPs were synthesized using the seed-mediated growth method. Briefly, 15 mL of 1% (w/v) sodium citrate was mixed with boiling 1 mM $HAuCl_4$ solution for 15 m and served as the gold seed solution. Five milliliters of the solution was transferred into 500 mL of water with 500 mL of 1 M HCl and 1.25 mL of 100 mM $HAuCl_4$. The solution was vigorously stirred for 15 m, followed by adding 5 mL of 3 mM silver nitrate and 100 mM ascorbic acid. Finally, 10 mL of 1% sodium citrate was added to the solution, and the formed Au nanostars were stored at 4°C. Fe_3O_4 NPs were prepared by co-precipitation. In brief, a solution containing 2 mM $FeCl_3$ and 1 mM $FeCl_2$ was prepared in 180 mL of 0.04 M HCl. A 12.5 mL ammonia solution was added dropwise under a nitrogen atmosphere at 60°C for 30 m and stirred for 1 h to synthesize Fe_3O_4 NPs. The synthesized Fe_3O_4 NPs were collected with centrifugation at 8,000 rpm for 10 m, washed three times with deionized water, and stored at 4°C. Finally, the prepared Au and Fe_3O_4 NPs were mixed at a 2:1 weight ratio and incubated for 6 h. They were poured into ethanol, and the same volume of tetraethyl orthosilicate and ammonia solution was added and vigorously stirred for 2 h. The prepared Au-Fe_3O_4 silica NPs dispersion was washed with deionized water and incubated with the same volume of 3 g/200 mL polyvinyl pyrrolidone (PVP) solution overnight. The PVP-coated NPs were collected via centrifugation at 8,000 rpm for 10 m and stored at 4°C.

Characterization of Au-Fe_3O_4 silica NPs

UV-Vis-NIR absorption spectrum of Au-Fe_3O_4 silica NPs was characterized using a UV-Vis-NIR spectrophotometer (UV-3600 Plus; Shimadzu Corp., Japan). The hydrodynamic size and zeta potential were detected using a particle size analyzer (Nano ZSE, Malvern, UK). The morphology and particle size were also characterized using transmission electron microscopy (TEM) (Tecnai F20; FEI, USA). The powder X-ray diffraction (XRD) pattern was measured using an X-ray diffractometer (X'Pert PRO MPD; Malvern Panalytical, Netherlands). *In vitro* PAI and MRI signal of the NPs were investigated using a Vevo 3100 imaging system (FUJIFILM VisualSonics, Canada) and 3T magnetic resonance scanner (Spectra; Siemens, Germany), respectively. Magnetic responsiveness of the NPs was demonstrated using a magnet. Additionally, the NPs were incubated with H_2O, phosphate buffer solution (PBS), Dulbecco's modified Eagle medium (DMEM; Gibco, USA), or fetal bovine serum (FBS) (Gibco) for 1 week. The absorbance at 785 nm in different incubations was measured using the UV-Vis-NIR spectrophotometer every 24 h to determine NPs stability.

Preparation, culture, and identification of BM-MSCs

BM-MSCs were provided by the Ophthalmology Laboratory, the Chinese PLA General Hospital, China. Sprague Dawley rats were sacrificed by excessive anesthesia with 3% pentobarbital sodium (100 mg/kg), and their limbs were harvested. Bone marrow was flushed from the limbs with 4 g/L glucose DMEM culture medium (Gibco) supplemented with heparin (Sigma-Aldrich, China) and filtered using a 40 μm cell strainer (Corning Inc., USA). The cell suspension was added to a Percoll solution (Solarbio, China) at a 2:1 volume ratio. After 20 m centrifugation at 1,000 rpm, the middle-layer cells were collected and washed twice with 1 mL PBS. The cells were cultured at 3×10^5 cells/cm^2 density in DMEM containing 10% FBS and 1% penicillin/streptomycin (Gibco) at 37°C and 5% CO_2 in a cell incubator (Thermo, USA).

BM-MSCs were identified by the expression of CD44, CD73, CD90, CD45, CD11b, and CD29 markers. In brief, PE-CD44, PE-CD73, PE-CD90, PE-CD45, APC-CD11b, and APC-CD29 antibodies (BD Bioscience, USA) were incubated with third-generation BM-MSCs for 2 h and the cells were washed three times with 1 mL PBS. Expression of the MSC markers was assayed by flow cytometry (FACSCanto; BD Bioscience).

Differentiation efficiency and viability of BM-MSCs labeled with Au-Fe_3O_4 silica NPs in vitro

Third-generation BM-MSCs were seeded in 96-well plates at a concentration of 2×10^4–1×10^5 cells per well. For NPs labeling, BM-MSCs were incubated with serially concentrated (0.5, 1.0, 2.0, 3.0, 4.0, and 5.0 OD) Au-Fe_3O_4 silica NPs. After 24 h incubation, the labeled BM-MSCs were washed three times with fresh DMEM, and viability was determined with a CCK-8 assay (Shanghai Yisheng Biotechnology Co., Ltd, China). The cells were washed three times and incubated with a fresh culture medium containing 10% (v/v) CCK-8 solution. After 4 h, absorbance at 450 nm was measured with a microplate reader (SpectraMax 190; Molecular Devices, USA) under dark conditions.

Following a general procedure, the samples were prepared using nitric acid (electronic grade) after 12 h and 24 h incubation. The Au and Fe content of BM-MSCs was measured using an inductively coupled plasma mass spectrometer (ICP-MS) (NexION 300 ICP-MS; PerkinElmer, USA). Additionally, the labeled BM-MSCs were visualized by Prussian blue staining and observed with an inverted phase-contrast microscope (WMS-1083; Shanghai Wumo Optical Instrument Co., Ltd, China). CD44, CD73, CD90, CD45, CD11b, and CD29 expression was assayed by staining procedures described above to validate potential phenotypic changes of the labeled BM-MSCs.

Labeled BM-MSCs were stained with alizarin red and oil red O to determine their osteogenic and adipogenic potential. The steps began with incubation of BM-MSCs in a 6-well plate with Au-Fe_3O_4 silica NPs. After 24 h, the wells were washed with 2 mL PBS to remove excess NPs. The labeled BM-MSCs underwent adipogenesis and osteogenesis induction (adipogenic inducers: indomethacin 0.2 mmol/L, dexamethasone 1 mmol/L, IBMX 50 mmol/L, insulin 10 mg/L and osteogenic inducers: ascorbic acid 50 mmol/L, β-sodium glycerophosphate 1 mol/L, and dexamethasone 1 mmol/L). After induction, BM-MSCs were fixed with 4% formaldehyde at 20–25°C for 30 m. After washing three times with double distilled H_2O (ddH_2O), BM-MSCs were incubated for 3 to 4 m with 2% alizarin red S solution at room temperature, rinsed with ddH_2O, and osteogenic differentiation was evaluated by light microscopy. For oil red O staining, labeled BM-MSCs were treated with 60% isopropanol for 5 m, incubated in oil red O solution for 5 m, and rinsed with ddH_2O. Adipogenic differentiation was observed by light microscopy.

Rat model of LC

The animal experimental protocol was approved by the Institutional Animal Care and Use Committee of the Chinese PLA General Hospital. Male Sprague Dawley rats weighing from 400 g to 450 g were provided by the Laboratory Animal Center of the Chinese PLA General Hospital. They were injected intraperitoneally with 40% CCl_4 in olive oil for 8 weeks to establish the LC model. The first CCl_4 dose was 5 mL/kg, and subsequent doses were 3 mL/kg administered every 3 days. Rats were starved for 8 to 12 h before each administration.

Administration routes

Rats with LC were randomly divided into three experimental groups depending on the administration route, controls (n=10), hepatic artery injection (n=10), and tail vein injection (n=10). The rats were anesthetized, and the skin of the right inguinal region was disinfected. A 1.5 F microcatheter (Medtronic; CA, USA) was introduced into the exposed femoral artery using a 22 G indwelling needle (Braun, Malaysia) and inserted into the common hepatic artery under the guidance of digital subtraction angiography (Miyabi System; Siemens, Artris Zee, Germany and Allura Xper FD20; Philips, Netherlands). Subsequently, the labeled BM-MSCs suspension was injected into the hepatic artery through the catheter (1×10^7/mL BM-MSCs in 1 mL saline). Intramuscular injections of penicillin (300,000 U per rat, Chinese medicine) was administered for anti-infection treatment for 3 days after surgery. For tail vein injection, the same amount of labeled BM-MSCs was injected into the tail vein of rats through a 24 G indwelling needle (Braun, Malaysia) under anesthesia. After injection, the puncture site was pressed with gauze for 10 m to prevent bleeding.

Detection of NPs-labeled BM-MSCs in liver with MRI and PAI

The distribution of labeled BM-MSCs in the liver of rats with LC was tracked using a 7T nuclear magnetic scanner (Varian, USA) before and after the injection (1, 6, 24, and 72 h). The rats were scanned in the prone position using an abdominal coil. The scanning parameters were repetition time, 3,000 ms; time of echo, 36 ms; layers, 10; layer thickness, 2 mm; layer spacing, 0.5 mm; and 256×256 pixels.

A PAI system (Nexus 128 Fully 3D Photoacoustic CT Scanner; Endra, USA) was used to detect the distribution of NPs-labeled BM-MSCs in the livers of rats from each experimental group. The anesthetized rats were scanned in the prone position. The liver was placed in the center of the detection field. The detection parameters were an excitation wavelength of 785 nm; angle of 120°, pulse 30, field of view 256×256, voxel 100 μm, and a window width 50–500.

Detection of NPs-labeled BM-MSCs in vivo with pathological assays

Four rats per group were sacrificed 72 h after administration. Major organs such as the heart, liver, lung, and kidney were harvested, fixed, and cut into 5 μm tissue sections and stained with Prussian blue. The distribution of labeled BM-MSCs was observed by microscopy (WMS-1083; Shanghai Wumo Optical Instrument Co., Ltd, China).

Statistical analysis

Statistical data analysis was performed with SPSS software version 22.0 (IBM Corp., USA). Data were reported as means±standard deviations and compared by one-way analysis of variance. Results were considered statistically significant when p was <0.05.

Results

Characterization of Au-Fe_3O_4 silica NPs

Au-Fe_3O_4 silica NPs were established by combining star-shaped Au NPs and Fe_3O_4 NPs. As shown in Figure 1A, Au-Fe_3O_4 silica NPs showed obvious absorbance at approximately 880 nm due to the presence of star-shaped NPs, which is crucial for PAI. The zeta potential was −12 mV (Fig. 1B), indicating that Au NPs (41.5 mV) and Fe_3O_4 NPs (−29.7 mV) were successfully incorporated into the silica layer. They also had a hydrodynamic size of approximately 300 nm. The result is consistent with the TEM images (Fig. 1C-E) that showed Au-Fe_3O_4 silica NPs consisted of a star-shaped Au core and an exterior silica layer doped with Fe_3O_4 NPs (Fig. 1E). Typical diffraction peaks of Fe_3O_4 NPs and Au NPs in the XRD images further confirmed the incorporation of Au and Fe_3O_4 in the hybrid NPs system (Fig. 1F).

Increasing PAI signal intensity was positively correlated with the concentration of Au-Fe_3O_4 silica NPs (Fig. 2A, Table 1). The measured MRI signal intensities at different NPs concentrations (0, 0.01, 0.02, 0.03, 0.04, and 0.05 OD) (Fig. 2B, Table 2) also revealed that the T_2 relaxation rate ($1/T_2$) was linearly related to NPs concentration. In addition, the NPs were entirely attracted to the side of the magnet when it was placed on one side of the Au-Fe_3O_4 silica NPs suspension, indicating their quick magnetic responsiveness (Fig. 2C). The high stability of Au-Fe_3O_4 silica NPs in various solutions (e.g., H_2O, PBS, DMEM, and FBS, Fig. 2D) was confirmed as they had a constant absorbance of approximately 0.6 OD. The results demonstrate that Au-Fe_3O_4 silica NPs could be visualized by both PAI and MRI.

Biocompatibility and labeling efficiency of Au-Fe_3O_4 silica NPs

BM-MSCs were generated from the bone marrow of Sprague Dawley rats and cultured for three generations (Fig. 3A). After incubating them for 24 h with Au-Fe_3O_4 silica NPs at 0.5, 1.0, 2.0, 3.0, 4.0, and 5.0 OD, their viability was 98.43%±1.59%,87.62%±1.34%,77.91%±5.86%,65.57%±12.8%,60.91%±5.11%, and 42.43%±6.13% (P_{trend}<0.001), respectively. More than 80% of BM-MSCs were viable when the Au-Fe_3O_4 silica NPs concentration was lower than 2.0 OD, which illustrated good biocompatibility (Fig. 3B, Table 3).

After coincubating BM-MSCs with Au-Fe_3O_4 silica NPs at a concentration of 2.0 OD for 24 h, the Au uptake at 0 h, 12 h, and 24 h was (13.48±0.96) μg/mL, (14.66±0.59) μg/mL, and (22.65±1.82) μg/mL (p<0.05), respectively (Fig. 3C, Table 4). Fe uptake at 0 h, 12 h, and 24 h was (125.52±4.47) μg/mL, (140.82±10.37) μg/mL, and (234.03±11.47) μg/mL (p<0.05), respectively. The results indicate that 24 h coincubation significantly increased the uptake of Au-Fe_3O_4 silica NPs. Moreover, Prussian blue staining *in vitro* confirmed that BM-MSCs take up more Au-Fe_3O_4 silica NPs after 24 h incubation (Fig. 3D). TEM results showed that Au-Fe_3O_4 silica NPs remained inside the BM-MSCs for 96 h after labeling (Fig. 3E).

Expression levels of CD44, CD73, CD90, CD29, CD45, and

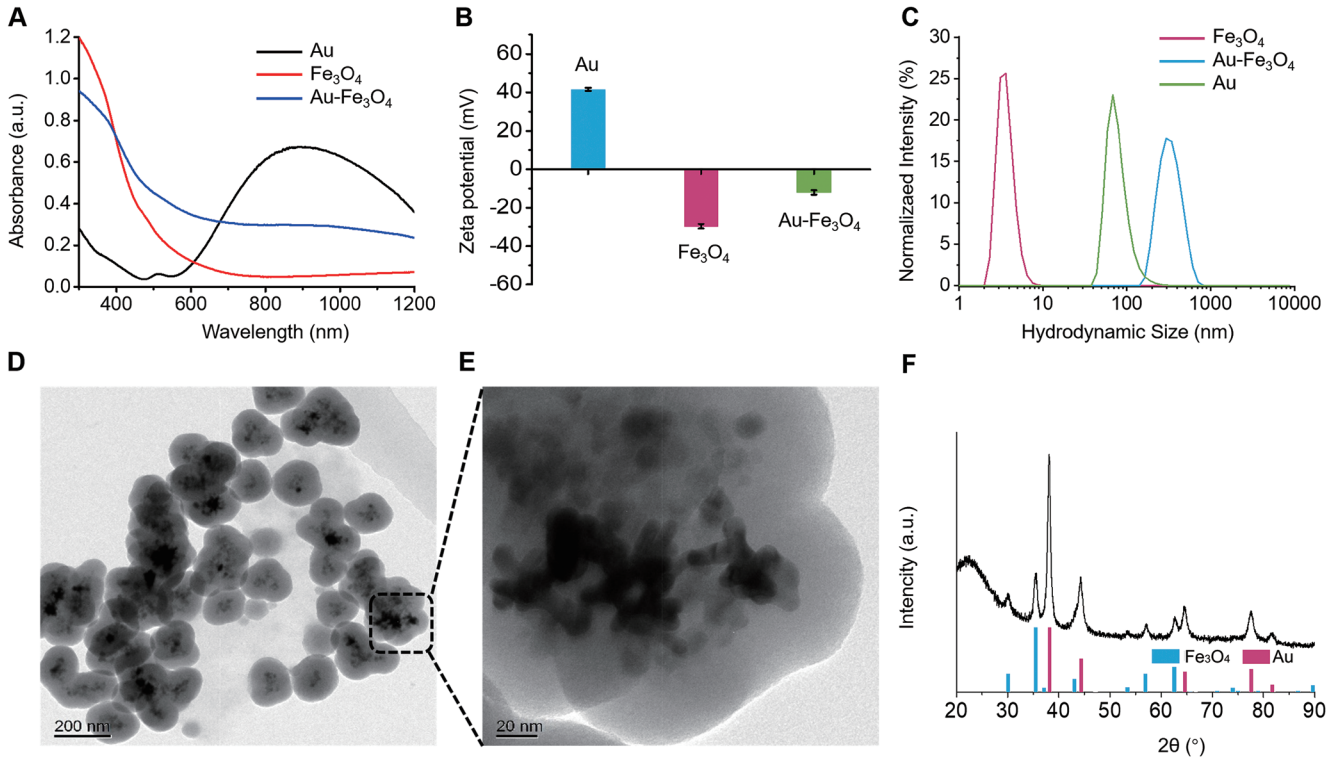

Fig. 1. Characterization of Au-Fe_3O_4 silica NPs. (A) The UV-Vis-NIR absorbance of Au-Fe_3O_4 silica NPs. Au-Fe_3O_4 silica NPs show obvious absorbance at approximately 880 nm due to the presence of star-shaped Au NPs. (B) Zeta potential of Au-Fe_3O_4 silica NPs is −12 mV, indicating Au NPs (41.5 mV) and Fe_3O_4 NPs (−29.7 mV) are successfully incorporated into the silica layer. (C) The hydrodynamic size of Au-Fe_3O_4 silica NPs is approximately 300 nm. (D–E) TEM images of Au-Fe_3O_4 silica NPs reveal a star-shaped Au core and an outside silica layer doped with Fe_3O_4 NPs. (F) The X-ray diffraction pattern of Au-Fe_3O_4 silica NPs confirms the incorporation of Au and Fe_3O_4 in the NPs system. NPs, nanoparticles; UV-Vis-NIR, ultraviolet-visible-nearinfrared; TEM, transmission electron microscopy.

CD11b on the surface of BM-MSCs were 97.81%, 99.27%, 99.56%, 99.67%, 0.55% and 1.15%, respectively. After co-incubating the cells with Au-Fe_3O_4 silica NPs (2.0 OD) for 24 h, the expression levels were 99.06%, 98.07%, 97.38%, 97.95%, 0.27%, and 0.10%, respectively. (Fig. 4A-H), indicating that labeling BM-MSCs with Au-Fe_3O_4 silica NPs did not alter the expression of stem cell surface markers. Moreover, labeled BM-MSCs did not have a significant decrease in cell proliferation at 7 days (p>0.05; Fig. 4I, Table 5). Similar to the control (BM-MSCs), after adipogenesis and osteogenesis, induction of Au-Fe_3O_4 silica NPs-labeled BM-MSCs, oil red O and alizarin red staining results showed significant intracellular lipid droplets and calcium salt deposition (Fig. 4J).

MRI/PAI dual-modal imaging features of rat liver after administering NPs-labeled BM-MSCs

For the hepatic artery group, T_2-weighted images showed a patchy hypointense (dark) signal in the rat liver, 1 and 6 h after injecting with Au-Fe_3O_4 silica NPs-labeled BM-MSCs. Subsequently, the hypointense signal gradually diffused within 72 h (Fig. 5A). A similar trend was observed on PA images, where the localized hyperintensity in the liver 1 h after administration diffused within 72 h (Fig. 5B). In the tail vein group, T_2-weighted images revealed a star-shaped hypointense signal in the liver 24 h post-injection and diffuse hypointensity after 72 h (Fig. 5A). Similarly, the photoacoustic signal of the liver gradually increased within 72 h after injection with the labeled BM-MSCs. (Fig. 5B). Furthermore, Prussian blue staining confirmed the results of MRI and PAI imaging (Fig. 6). The labeled BM-MSCs were visible in the liver of both experimental groups compared to control and accumulated in the lung (Fig. 7A). The blue staining was observed neither in the heart nor kidneys of both groups (Fig. 7B, C). In contrast to that in the tail vein group, 72 h after the infusion of labeled BM-MSCs in the hepatic artery group, blue-stained BM-MSCs were not only distributed in the portal area but were also clearly seen in the fibrous septa (Supplementary Fig. 1).

One month after the infusion of Au-Fe_3O_4 silica NPs-labeled BM-MSCs by each route in each group of rats, liver function and fibrosis-related hematological indexes aspartate aminotransferase (AST), albumin (ALB), hyaluronic acid, and IV collagen fibrosis improved significantly in the hepatic artery group compared with that in the tail vein group (p<0.05; Supplementary Fig. 2A, Table 6). Masson staining results showed that the fibrous septa in the liver tissue of rats in the hepatic artery group were significantly narrower, and the degree of liver fibrosis was significantly improved compared with that in the tail vein group (Supplementary Fig. 2B).

Discussion

The USA Food and Drug Administration has approved more than 60 clinical studies on therapeutic MSCs, suggesting good prospects for treating many diseases, including cartilage injury, diabetes, and diabetic foot.[19–23] However, the distribution, migration, and destination of MSCs *in vivo* remain unclear. Therefore, real-time imaging-guided tracking of infused MSCs *in vivo* is necessary to explore their safety, efficacy, and mechanism in treating LC. Fluo-

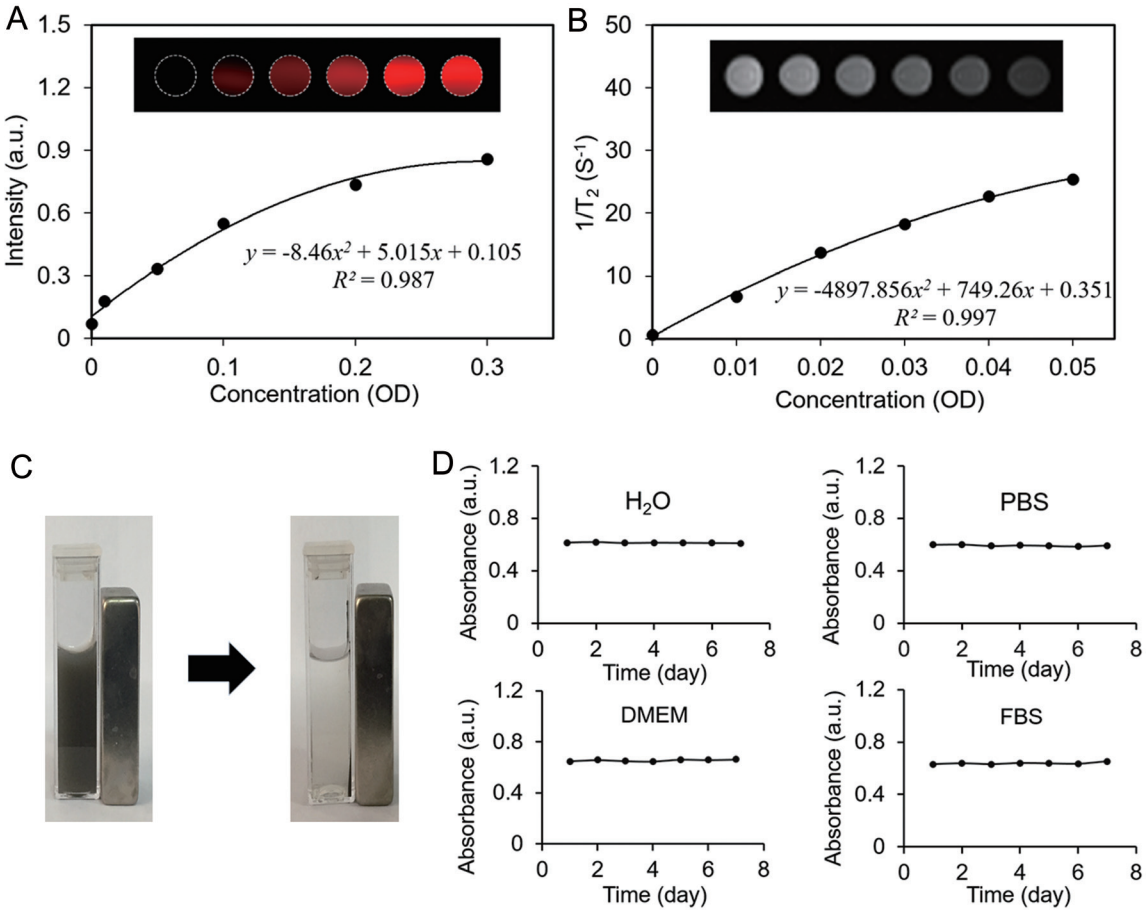

Fig. 2. Properties of Au-Fe_3O_4 silica NPs. (A) PA images of Au-Fe_3O_4 silica NPs. The increasing signal intensity positively correlates with the NPs concentration. (B) T_2-weighted MR images of Au-Fe_3O_4 silica NPs. The T_2 relaxation rate ($1/T_2$) is linearly related to the NPs concentration. (C) Magnetic responsiveness of Au-Fe_3O_4 silica NPs. The Au-Fe_3O_4 silica NPs are entirely attracted to the side of the magnet. (D) Stability of Au-Fe_3O_4 silica NPs in H_2O (top left), PBS (top right), DMEM (bottom left), and FBS (bottom right). The absorbance of Au-Fe_3O_4 silica NPs in the solutions is maintained at 0.6 OD for up to one week. NPs, nanoparticles; PA, photoacoustic; MR, magnetic resonance; PBS, phosphate buffered saline; DMEM, Dulbecco's modified Eagle's medium; FBS, fetal bovine serum; OD, optical density.

rescent and genetic markers are used to track therapeutic stem cells. However, *in vivo* precise tracking of stem cells labeled with fluorescent markers is challenging because of poor penetration depth of fluorescence and high background noise from tissues. Various biomedical imaging tools such as magnetic particle imaging, computed tomography, positron-emission tomography, and MRI are employed for cell tracking *in vitro* and *in vivo*.[24–27] For example, MRI is a hot spot in stem cell tracking owing to its characteristics of noninvasiveness, low toxicity, and high labeling efficiency of magnetic iron oxide particles. However, low spatial resolution and poor sensitivity limit the applicability of MRI. High resolution and high contrast of PAI effectively compensate for the disadvantages of MRI. Therefore, composite NPs with multimodal imaging abilities improve labeling efficiency and allow accurate *in vivo* stem cell tracking. In our study, Au-Fe_3O_4 silica NPs were composed of MRI contrast-enhancing Fe_3O_4 NPs and photoacoustic-enhancing Au NPs, which provided a new noninvasive *in vivo* dual-modal imaging method for stem cell tracking. The results of CCK-8 assays, ICP, Prussian blue staining, phenotypic characterization, and adipogenesis and osteogenesis induction demonstrated that 24 h coincubation with Au-Fe_3O_4 silica NPs at an optical density of 2.0 OD safely and efficiently labeled BM-MSCs. The study also verified the feasibility of noninvasive monitoring of BM-MSCs *in vivo* using multimodal imaging (MRI and PAI) after injecting rats with BM-MSCs labeled with Au-Fe_3O_4 silica NPs. Under the action of Fe_3O_4 NPs and Au NPs, the liver showed hypointensity on T_2-weighted images and hyperintensity on PAI. In addition, Zhou Bin *et al*.[28] found that stem cells eliminate superparamagnetic iron oxide (SPIO) when SPIO-labeled BM-MSCs enter the body. That phenomenon has implications for MRI tracking

Table 1. The signal intensity (a.u.) of Au-Fe_3O_4 silica NPs in PA images (Fig. 2A)

Concentration (OD)	0	0.01	0.05	0.1	0.2	0.3
Intensity (a.u.)	0.07	0.18	0.33	0.55	0.74	0.86

NPs, nanoparticles; PA, photoacoustic; OD, optical density.

Table 2. The $1/T_2$ (s^{-1}) of Au-Fe_3O_4 silica NPs in T_2-weighted MR images (Fig. 2B)

Concentration (OD)	0	0.01	0.02	0.03	0.04	0.05
$1/T_2$ (s^{-1})	0.62	6.73	13.76	18.29	22.73	25.42

NPs, nanoparticles; MR, magnetic resonance; OD, optical density.

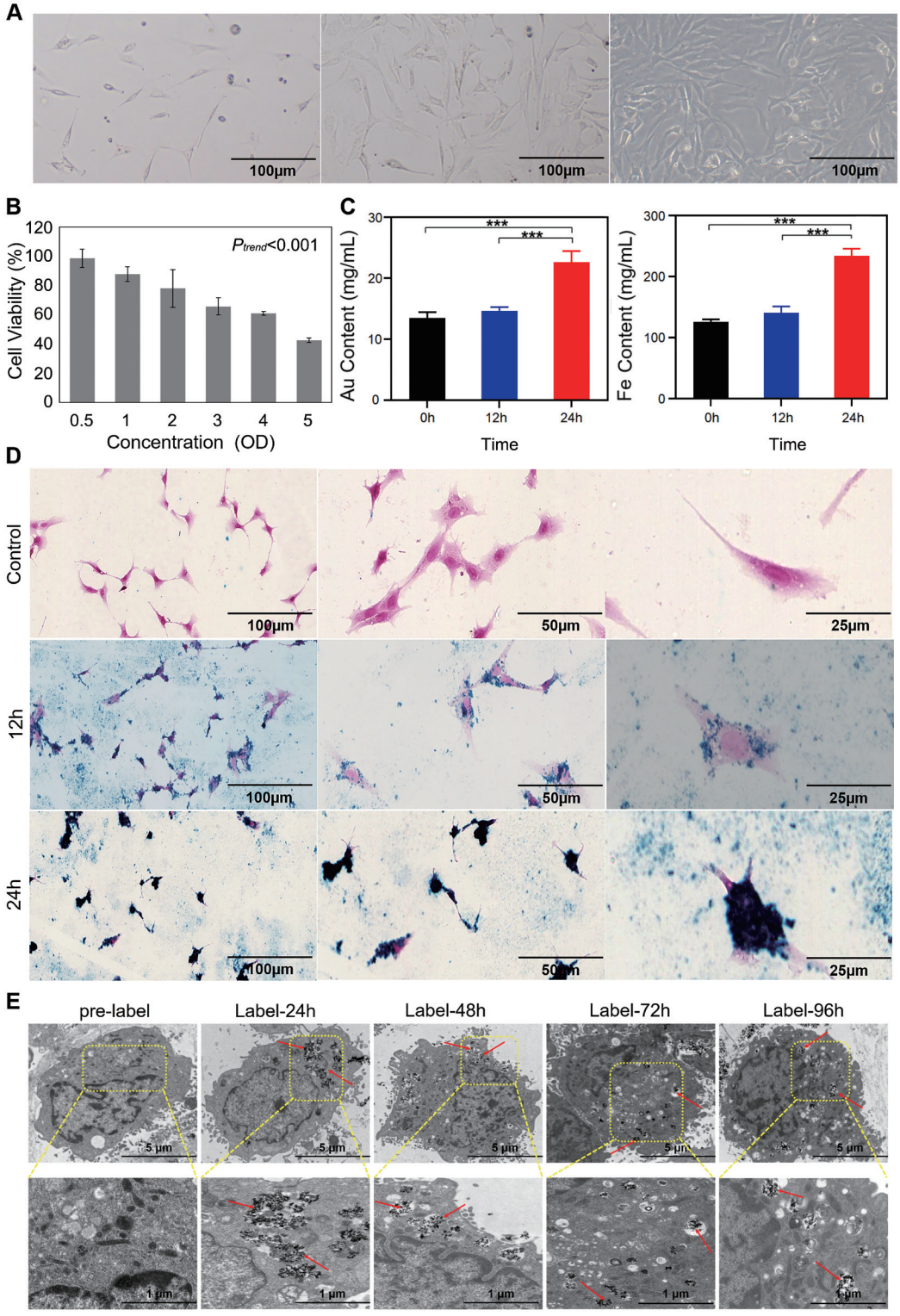

Fig. 3. Labeling efficiency of Au-Fe_3O_4 silica NPs. (A) The morphology of BM-MSCs after 1, 2, and 3 days. (B) The viability of BM-MSCs after incubation with various concentrations of Au-Fe_3O_4 silica NPs for 24 h. More than 80% BM-MSCs are viable when the NPs concentration is lower than 2.0 OD. (C) The results of ICP-MS assays depict Au (left) and Fe (right) content (mg/mL) in BM-MSCs after incubating them with Au-Fe_3O_4 silica NPs for 0 h, 12 h, or 24 h. The Au and Fe uptake significantly increases after 24 h incubation. (D) The Prussian blue staining of BM-MSCs after 12 h or 24 h incubation with Au-Fe_3O_4 silica NPs. The cells take up more Au-Fe_3O_4 silica NPs after 24 h incubation. (E) Transmission electron microscopy results show that Au-Fe_3O_4 silica NPs were inside cells 96 h after labeling BM-MSCs. Red arrows show Au-Fe_3O_4 silica NPs inside BM-MSCs. ***p<0.001. NPs, nanoparticles; BM-MSCs, bone marrow-derived mesenchymal stem cells; OD, optical density; ICP-MS, inductively coupled plasma mass spectrometry.

Table 3. Viability of BM-MSCs after incubation with various concentrations of Au-Fe_3O_4 silica NPs (*n*=5; Fig. 3B)

Concentration (OD)	0.5	1.0	2.0	3.0	4.0	5.0
Cell viability (%)	98.43±1.59	87.62±1.34	77.91±5.86	65.57%±12.8	60.91±5.11	42.43±6.13

BM-MSCs, bone marrow-derived mesenchymal stem cells; NPs, nanoparticles; OD, optical density.

Table 4. Results of ICP-MS assays to depict Au and Fe content in BM-MSCs after incubation with Au-Fe_3O_4 silica NPs at a concentration of 2.0 OD (*n*=3; Fig. 3C)

	0 h	12 h	24 h
Au (μg/mL)	13.48±0.96	14.66±0.59	22.65±1.82
Fe (μg/mL)	125.52±4.47	140.82±10.37	234.03±11.47

ICP-MS, inductively coupled plasma mass spectrometry; BM-MSCs, bone marrow-derived mesenchymal stem cells; NPs, nanoparticles; OD, optical density.

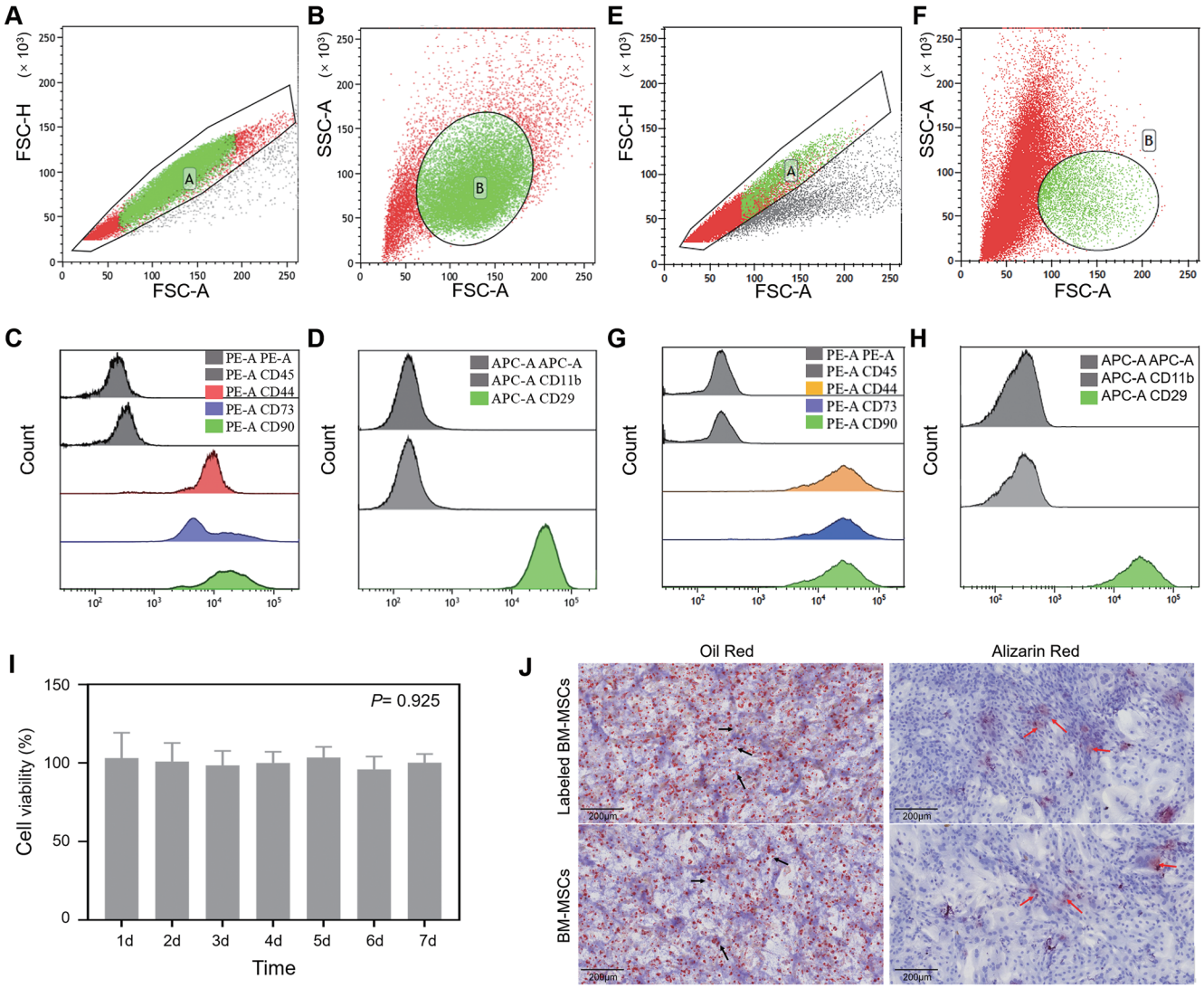

Fig. 4. Biocompatibility of BM-MSCs after Au-Fe_3O_4 silica NPs labeling. (A–D) The expression of stem cell surface markers before labeling BM-MSCs with Au-Fe_3O_4 silica NPs. The expression of CD44, CD73, CD90, and CD29 is high, while that of CD45 and CD11b is low. (E–H) The expression of stem cell surface markers after labeling BM-MSCs with Au-Fe_3O_4 silica NPs. The expression of BM-MSC cell surface markers does not change after Au-Fe_3O_4 silica NPs labeling. (I) Labeled BM-MSC proliferation and viability levels. When Au-Fe_3O_4 silica NPs were labeled, the proliferation and viability of BM-MSCs did not show a significant decrease in 7 days. (J) Au-Fe_3O_4 silica NPs-labeled BM-MSCs for adipogenesis and osteogenesis induction. Similar to the control (BM-MSCs), Oil red O staining was visible as red lipid droplets inside the labeled BM-MSCs and Alizarin red staining shows calcium salt deposition inside the labeled BM-MSCs. NPs, nanoparticles; BM-MSCs, bone marrow-derived mesenchymal stem cells.

Table 5. Proliferation and viability of BM-MSCs after Au-Fe_3O_4 silica NPs labeling (*n*=4; Fig. 4I)

Time, days	1	2	3	4	5	6	7
Cell viability (%)	103.00±16.37	101.00±11.86	98.25±9.14	99.75±7.14	103.50±6.81	95.50±8.23	99.75±5.74

BM-MSCs, bone marrow-derived mesenchymal stem cells; NPs, nanoparticles.

of stem cells *in vivo*. In this study, we observed that Au-Fe_3O_4 silica NPs can effectively remain inside the cell for 96 h after labeling via TEM, whereas BM-MSCs can maintain high viability. Therefore, when Au-Fe_3O_4 silica NPs-labeled BM-MSCs enter the body, the accurate tracing of BM-MSCs but not other cells, such as Kupffer cells, can be achieved for at least 96 h of dual-modal imaging.

Peripheral vein and the hepatic artery are the main routes of injecting stem cells for treating LC in clinical settings. However, different administration routes affect the migration and distribution of stem cells. Cai *et al.*[29] injected cirrhotic rats with MSCs labeled with SPIONs through the hepatic artery. The liver showed negative enhancement on T_2-weighted images after 1 h, 3 days, and 7 days. In addition, the T_2 signal intensity of the liver dropped substantially 1 h after injection and gradually increased after

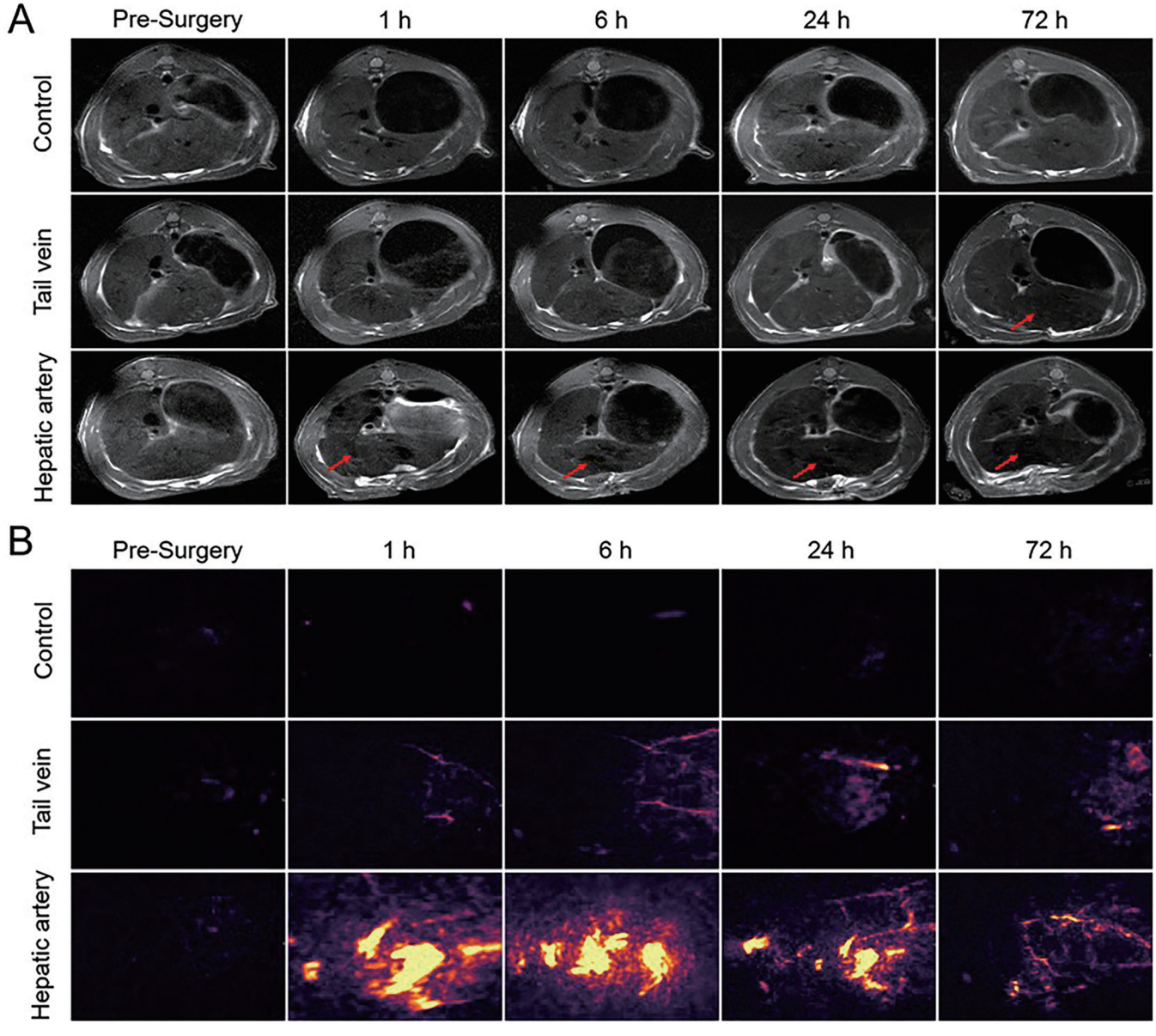

Fig. 5. MRI/PAI dual-modal imaging of the rat liver. (A) MRI T_2-weighted images reveal the hypointense signal (red arrows) in the liver of two rat groups at different time points after injecting with BM-MSCs labeled with Au-Fe_3O_4 silica NPs via the hepatic artery or tail vein compared to the control. (B) PA imaging shows the hyperintensity in the liver of rat groups injected with the labeled BM-MSCs via the hepatic artery or tail vein compared to the control. NPs, nanoparticles; BM-MSCs, bone marrow-derived mesenchymal stem cells; MRI, magnetic resonance imaging; PA, photoacoustic.

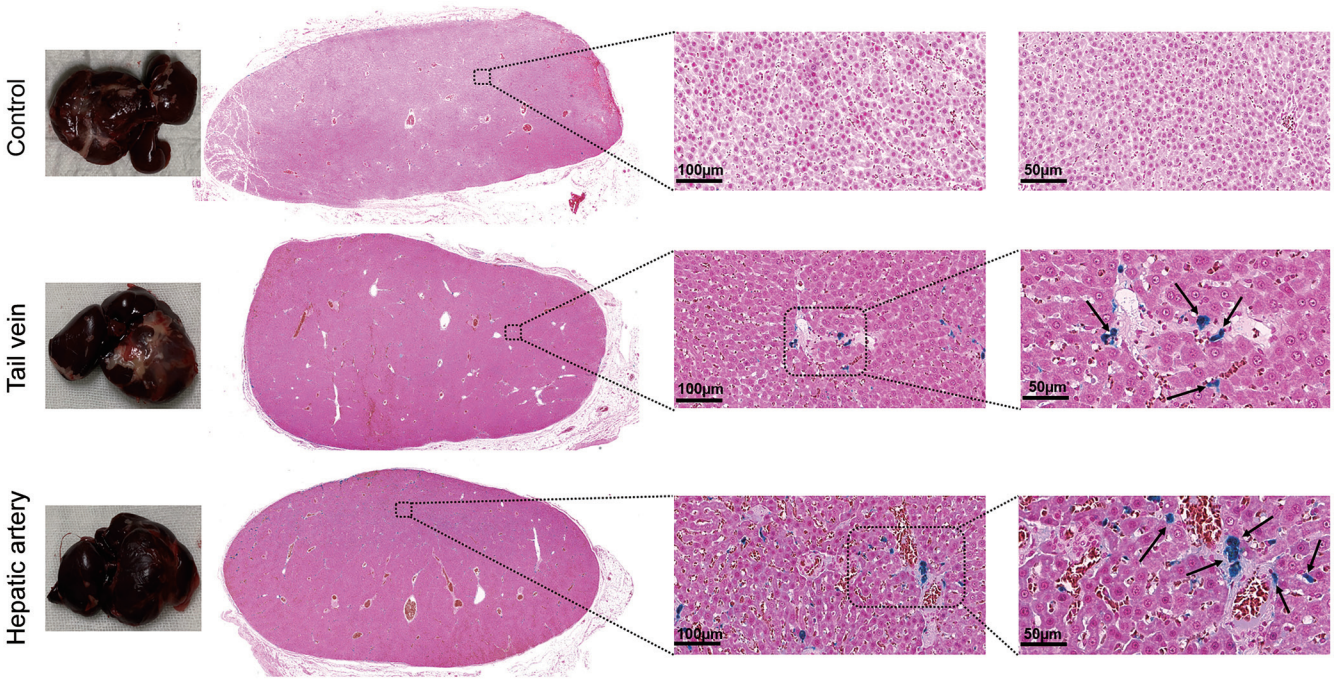

Fig. 6. Prussian blue staining of the rat liver 72 h after administering BM-MSCs labeled with Au-Fe_3O_4 silica NPs. Aggregation of NPs-labeled BM-MSCs is increased in the livers of rats administered the labeled cells via the hepatic artery compared with the livers of rats administered via the tail vein. BM-MSCs labeled with Au-Fe_3O_4 silica NPs are blue-stained (black arrows). NPs, nanoparticles; BM-MSCs, bone marrow-derived mesenchymal stem cells.

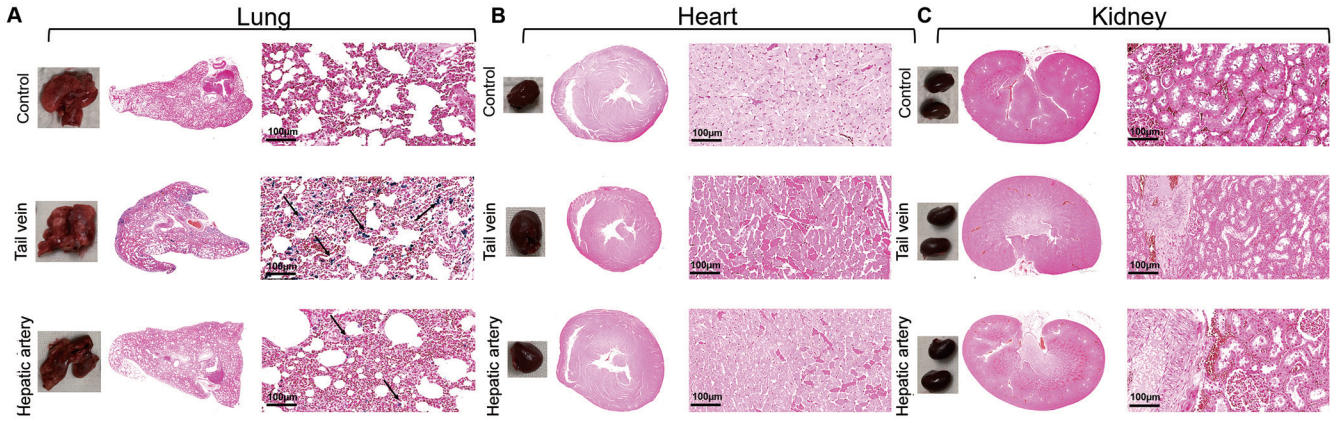

Fig. 7. Histological assays of other major organs after administration of BM-MSCs labeled with Au-Fe_3O_4 silica NPs for 72 h. Higher aggregation of NPs-labeled BM-MSCs is present in the lung (A) of rats administered the labeled cells via the tail vein than in the lung of rats administered via the hepatic artery. BM-MSCs labeled with NPs are observed neither in the heart (B) nor kidneys (C) of both groups. BM-MSCs labeled with Au-Fe_3O_4 silica NPs are blue-stained (black arrows). NPs, nanoparticles; BM-MSCs, bone marrow-derived mesenchymal stem cells.

Table 6. Liver function and fibrosis-related hematological indexes of rats in each group 1 month after infusion of BM-MSCs (*n*=6; Supplementary Fig. 2A)

	Control	Tail vein	Hepatic artery
AST (U/L)	164±8.29	143.5±13.55	124±11.47
ALT (U/L)	81±4.47	71±4.15	65.83±2.48
ALB (g/L)	31.92±1.03	34.93±0.73	38.33±0.79
TBIL (μmol/L)	23.65±3.54	16.47±3.15	13.78±2.18
hyaluronic acid (ng/mL)	110.88±10.79	93.85±3.17	80.41±7.07
IV collagen fibers (ng/mL)	38.22±2.84	27.06±3.24	20.17±3.59

AST, aspartate aminotransferase; ALT, alanine aminotransferase; ALB, albumin; TBIL, total bilirubin.

3 days. These findings indicate that MSCs injected through the hepatic artery preferably accumulate in the liver. The number of MSCs in the liver eventually decreased because of extrahepatic migration and intrahepatic stem cell death. Eggenhofer *et al*[30] found that most MSCs (60%) primarily accumulate in the lung after being injected through the tail vein, aggregating in the liver 24 h later. Moreover, Gholamrezanezhad *et al*[31] confirmed that BM-MSCs immediately aggregate in the lung after intravenous injection and gradually migrate to the liver. In our study, signal characteristics of the liver revealed by dual-modal MRI/PAI imaging after injecting BM-MSCs labeled with Au-Fe_3O_4 silica NPs through either the hepatic artery or tail vein were similar to those reported by previous studies of the distribution and migration of stem cells.

With regard to the mechanism of stem cell therapy for LC, previous studies have shown that when stem cells enter the body, they primarily home to the liver. Subsequently, the stem cells gradually differentiate into hepatocytes and replace the diseased cells. At the same time, stem cells inhibit the process of liver fibrosis through mechanisms such as mediating immune regulation to alleviate the inflammatory response and remodeling the extracellular matrix.[32–34] In this study, we observed that BM-MSCs aggregated more in the liver in the hepatic artery group than in the tail vein group 72 h after the infusion of labeled BM-MSCs. Moreover, a significant distribution of BM-MSCs were observed in the fibrous septa. The reason may be that the infusion of BM-MSCs via the hepatic artery route avoids the systemic circulation and increases the aggregation of BM-MSCs in the liver site and accelerates the homing of stem cells. We further found that some hematological indexes of liver function (AST and ALB), fibrosis (hyaluronic acid and type IV collagen fibers), and the degree of liver fibrosis (Masson staining) were significantly improved in the hepatic artery group compared with those in the tail vein group 1 month after BM-MSC infusion. The results confirm that the advantages of BM-MSC infusion via the hepatic artery would improve the effectiveness of stem cell therapy for LC. Therefore, the study found that the transhepatic arterial route was superior to the tail vein route for the treatment of LC with BM-MSCs. The limitation of our study is the lack of long-term validation data on the therapeutic effectiveness of BM-MSCs for the treatment of LC in rats, which should be the focus of future research.

Conclusions

In summary, we demonstrated that Au-Fe_3O_4 silica NPs were a precise MRI/PAI dual-modal imaging nanoplatform for tracking the distribution and migration of BM-MSCs injected through different routes into rats with LC. This high-precision stem cell tracking strategy can be applied to monitor stem cells in regenerative medicine. In addition, the transhepatic arterial infusion of BM-MSCs is the preferred route of administration for the treatment of liver cirrhosis.

Funding

This study was funded by grants from The National Natural Science Foundation of China (No. 81671800)

Conflict of interest

FSW has been an associate editor of *Journal of Clinical and Translational Hepatology* since 2013. The other authors have no conflict of interests related to this publication.

Author contributions

Conception and design (FSW), drafting of the manuscript (FYL), acquisition of data (FYL, XL), data analysis and interpretation (FYL, HJY, XMT, YMX, MZ), critical revision of the manuscript (MS), study supervision and final approval of the manuscript (FSW).

Ethical statement

The animal experimental protocol was approved by the Institutional Animal Care and Use Committee of the Chinese PLA General Hospital.

Data sharing statement

The datasets and figures used in support of the findings of this study are included within the article and supplementary information materials.

References

[1] Barnett R. Liver cirrhosis. Lancet 2018;392(10144):275. doi:10.1016/S0140-6736(18)31659-3, PMID:30064644.
[2] Garcia-Tsao G, Abraldes JG, Berzigotti A, Bosch J. Portal hypertensive bleeding in cirrhosis: risk stratification, diagnosis, and management: 2016 practice guidance by the American Association for the study of liver diseases. Hepatology 2017;65(1):310–335. doi:10.1002/hep.28906, PMID:27786365.
[3] Smith A, Baumgartner K, Bositis C. Cirrhosis: diagnosis and management. Am Fam Physician 2019;100(12):759–770. PMID:3184557.
[4] Hirao H, Nakamura K, Kupiec-Weglinski JW. Liver ischaemia-reperfusion injury: a new understanding of the role of innate immunity. Nat Rev Gastroenterol Hepatol 2022;19(4):239–256. doi:10.1038/s41575-021-00549-8, PMID:34837066.
[5] Karvellas CJ, Francoz C, Weiss E. Liver transplantation in acute-on-chronic liver failure. Transplantation 2021;105(7):1471–1481. doi:10.1097/TP.0000000000003550, PMID:33208692.
[6] Zhu M, Hua T, Ouyang T, Qian H, Yu B. Applications of mesenchymal stem cells in liver fibrosis: novel strategies, mechanisms, and clinical practice. Stem Cells Int 2021;2021:6546780. doi:10.1155/2021/6546780, PMID:34434239.
[7] El Agha E, Kramann R, Schneider RK, Li X, Seeger W, Humphreys BD, *et al*. Mesenchymal stem cells in fibrotic disease. Cell Stem Cell 2017;21(2):166–177. doi:10.1016/j.stem.2017.07.011, PMID:28777943.
[8] Mushahary D, Spittler A, Kasper C, Weber V, Charwat V. Isolation, cultivation, and characterization of human mesenchymal stem cells. Cytometry A 2018;93(1):19–31. doi:10.1002/cyto.a.23242, PMID:29072818.
[9] Chu DT, Phuong TNT, Tien NLB, Tran DK, Thanh VV, Quang TL, *et al*. An update on the progress of isolation, culture, storage, and clinical application of human bone marrow mesenchymal stem/stromal cells. Int J Mol Sci 2020;21(3):708. doi:10.3390/ijms21030708, PMID:31973182.
[10] Hong YY, Xu H, Yang Y, Zhou S, Jin A, Huang X, *et al*. Isolation and cultivation of mandibular bone marrow mesenchymal stem cells in rats. J Vis Exp 2020;162:e61532. doi:10.3791/61532, PMID:32925878.
[11] Brown C, McKee C, Bakshi S, Walker K, Hakman E, Halassy S, *et al*. Mesenchymal stem cells: cell therapy and regeneration potential. J Tissue Eng Regen Med 2019;13(9):1738–1755. doi:10.1002/term.2914, PMID:31216380.
[12] Cao Y, Ji C, Lu L. Mesenchymal stem cell therapy for liver fibrosis/cirrhosis. Ann Transl Med 2020;8(8):562. doi:10.21037/atm.2020.02.119, PMID:32775363.
[13] Tsuchiya A, Takeuchi S, Watanabe T, Yoshida T, Nojiri S, Ogawa M, *et al*. Mesenchymal stem cell therapies for liver cirrhosis: MSCs as "conducting cells" for improvement of liver fibrosis and regeneration. Inflamm Regen 2019;39(1):18. doi:10.1186/s41232-019-0107-z, PMID:31516638.
[14] Theruvath AJ, Nejadnik H, Lenkov O, Yerneni K, Li K, Kuntz L, *et al*. Tracking stem cell implants in cartilage defects of minipigs by using ferumoxytol-enhanced MRI. Radiology 2019;292(1):129–137. doi:10.1148/radiol.2019182176, PMID:31063081.
[15] Fang X, Lui KH, Li S, Lo WS, Li X, Gu Y, *et al*. Multifunctional nanotheranostic gold nanocage/selenium core-shell for PAI-guided chemo-photothermal synergistic therapy in vivo. Int J Nanomedicine 2020;15:10271–10284. doi:10.2147/IJN.S275846, PMID:33364758.
[16] Cai K, Zhang W, Foda MF, Li X, Zhang J, Zhong Y, *et al*. Miniature hollow gold nanorods with enhanced effect for in vivo photoacoustic imaging in the NIR-II window. Small 2020;16(37):e2002748. doi:10.1002/smll.202002748, PMID:32780938.
[17] Kang N, Xu D, Han Y, Lv X, Chen Z, Zhou T, *et al*. Magnetic targeting core/shell Fe_3O_4/Au nanoparticles for magnetic resonance/photoacoustic dual-modal imaging. Mater Sci Eng C Mater Biol Appl 2019;98:545–549. doi:10.1016/

j.msec.2019.01.013, PMID:30813057.
[18] Ma D, Shi M, Li X, Zhang J, Fan Y, Sun K, *et al*. Redox-sensitive clustered ultrasmall iron oxide nanoparticles for switchable T_2/T_1-weighted magnetic resonance imaging applications. Bioconjug Chem 2020;31(2):352–359. doi:10.1021/acs.bioconjchem.9b00659, PMID:31693856.
[19] Ross CL, Ang DC, Almeida-Porada G. Targeting mesenchymal stromal cells/pericytes (MSCs) with pulsed electromagnetic field (PEMF) has the potential to treat rheumatoid arthritis. Front Immunol 2019;10:266. doi:10.3389/fimmu.2019.00266, PMID:30886614.
[20] Mishra VK, Shih HH, Parveen F, Lenzen D, Ito E, Chan TF, *et al*. Identifying the therapeutic significance of mesenchymal stem cells. Cells 2020;9(5):1145. doi:10.3390/cells9051145, PMID:32384763.
[21] Cao Y, Gang X, Sun C, Wang G. Mesenchymal stem cells improve healing of diabetic foot ulcer. J Diabetes Res 2017;2017:9328347. doi:10.1155/2017/9328347, PMID:28386568.
[22] Moon KC, Suh HS, Kim KB, Han SK, Young KW, Lee JW, *et al*. Potential of allogeneic adipose-derived stem cell-hydrogel complex for treating diabetic foot ulcers. Diabetes 2019;68(4):837–846. doi:10.2337/db18-0699, PMID:30679183.
[23] Vizoso FJ, Eiro N, Costa L, Esparza P, Landin M, Diaz-Rodriguez P, *et al*. Mesenchymal stem cells in homeostasis and systemic diseases: hypothesis, evidences, and therapeutic opportunities. Int J Mol Sci 2019;20(15):3738. doi:10.3390/ijms20153738, PMID:31370159.
[24] Wu K, Su D, Liu J, Saha R, Wang JP. Magnetic nanoparticles in nanomedicine: a review of recent advances. Nanotechnology 2019;30(50):502003. doi:10.1088/1361-6528/ab4241, PMID:31491782.
[25] Kim D, Kim J, Park YI, Lee N, Hyeon T. Recent development of inorganic nanoparticles for biomedical imaging. ACS Cent Sci 2018;4(3):324–336. doi:10.1021/acscentsci.7b00574, PMID:29632878.
[26] Han X, Xu K, Taratula O, Farsad K. Applications of nanoparticles in biomedical imaging. Nanoscale 2019;11(3):799–819. doi:10.1039/c8nr07769j, PMID:30603750.
[27] Wang D, Zhang N, Jing X, Zhang Y, Xu Y, Meng L. A tumor-microenvironment fully responsive nano-platform for MRI-guided photodynamic and photothermal synergistic therapy. J Mater Chem B 2020;8(36):8271–8281. doi:10.1039/d0tb01373k, PMID:32812996.
[28] Zhou B, Li D, Qian J, Li Z, Pang P, Shan H. MR tracking of SPIO-labeled mesenchymal stem cells in rats with liver fibrosis could not monitor the cells accurately. Contrast Media Mol Imaging 2015;10(6):473–480. doi:10.1002/cmmi.1650, PMID:26153152.
[29] Cai J, Zhang X, Wang X, Li C, Liu G. In vivo MR imaging of magnetically labeled mesenchymal stem cells transplanted into rat liver through hepatic arterial injection. Contrast Media Mol Imaging 2008;3(2):61–66. doi:10.1002/cmmi.231, PMID:18381616.
[30] Eggenhofer E, Luk F, Dahlke MH, Hoogduijn MJ. The life and fate of mesenchymal stem cells. Front Immunol 2014;5:148. doi:10.3389/fimmu.2014.00148, PMID:24904568.
[31] Gholamrezanezhad A, Mirpour S, Bagheri M, Mohamadnejad M, Alimoghaddam K, Abdolahzadeh L, *et al*. In vivo tracking of ^{111}In-oxine labeled mesenchymal stem cells following infusion in patients with advanced cirrhosis. Nucl Med Biol 2011;38(7):961–967. doi:10.1016/j.nucmedbio.2011.03.008, PMID:21810549.
[32] Lee C, Kim M, Han J, Yoon M, Jung Y. Mesenchymal Stem Cells Influence Activation of Hepatic Stellate Cells, and Constitute a Promising Therapy for Liver Fibrosis. Biomedicines 2021;9(11):1598. doi:10.3390/biomedicines9111598, PMID:34829827.
[33] Li YH, Shen S, Shao T, Jin MT, Fan DD, Lin AF, *et al*. Mesenchymal stem cells attenuate liver fibrosis by targeting Ly6C$^{hi/lo}$ macrophages through activating the cytokine-paracrine and apoptotic pathways. Cell Death Discov 2021;7(1):239. doi:10.1038/s41420-021-00584-z, PMID:34518510.
[34] Saleh M, Fotook Kiaei SZ, Kavianpour M. Application of Wharton jelly-derived mesenchymal stem cells in patients with pulmonary fibrosis. Stem Cell Res Ther 2022;13(1):71. doi:10.1186/s13287-022-02746-x, PMID:35168663.